IEEE Access
Multidisciplinary | Rapid Review | Open Access Journal

Received February 10, 2022, accepted March 22, 2022, date of publication March 25, 2022, date of current version April 6, 2022.

Digital Object Identifier 10.1109/ACCESS.2022.3162260

Generation of a Flat-Top Magnetic Field With Multiple-Capacitor Power Supply

DAKE LI[1], HONGFA DING[1], YUCHAO FANG[2], SONG ZHANG[1], AND DAIYUAN PAN[1]

[1]Wuhan National High Magnetic Field Center, College of Electrical and Electronics Engineering, Huazhong University of Science and Technology, Wuhan 430074, China

[2]College of Electrical Engineering, Zhejiang University, Hangzhou 310027, China

Corresponding author: Hongfa Ding (dhf@hust.edu.cn)

This work was supported in part by the National Key Research and Development Program of China under Grant 2016YFA0401702, and in part by the National Natural Science Foundation of China under Grant 51821005/51507072.

ABSTRACT The flat-top magnetic field (FTMF) can meet scientific experimental requirements for higher magnetic intensity, longer flat-top pulse width, and lower ripple in physics, chemistry, biology, and other scientific fields. This paper proposes an FTMF system powered by the multiple-capacitor power supply (MCPS). The MCPS consists of several capacitor banks with customizable capacitance and given voltage. These banks discharge sequentially based on the designed time-series to yield an FTMF. Compared with other methods for generating the FTMF, the MCPS can easily generate FTMFs with high parameters and flexible adjustability of the pulse width. Due to the coupled variable parameters between and within the power supply and the magnet, a hybrid algorithm based on the genetic algorithm (GA) and particle swarm optimization (PSO) is applied to calculate the discharge parameters of the MCPS. The optimal solution from the GA-PSO hybrid algorithm is visualized and selected by the basis vector method. For verifying the effectiveness of the MCPS and the optimization method, a series of FTMFs at different magnetic field strength levels are modeled in MATLAB/Simulink and achieved in the experiment. The generated FTMF with the highest field strength is 50 T, its pulse width is 70 ms, and ripple is less than 0.7%.

INDEX TERMS Flat-top high magnetic field, multiple-capacitor power supply, multi-objective optimization, GA-PSO hybrid algorithm.

I. INTRODUCTION

Over the past decades, there has been a growing interest in the properties of substances and organisms under strong magnetic fields. Some scientific experiments such as the specific heat measurements and the nuclear magnetic resonance require higher magnetic field strength [1]–[4]. Compared with steady-state magnetic fields, the flat-top magnetic field (FTMF) has become an effective research method in these studies due to its relatively low energy cost and high peak magnetic field [5]. FTMFs with high magnetic field strength, long flat-top pulse width, and high stability are of great interest for scientific experiments [6]. Designing an FTMF system that meets the demand of scientific experiments is a great challenge for both power supply and magnet. In the case that the magnet satisfies the requirements for the heat capacity as well as the mechanical strength, the power supply is necessary to provide a high and stable output to the magnet during the period of flat-top. Therefore, much literature is focused on the power supply [7]–[10].

Nowadays, three types of power supplies are mainly applied in FTMF systems: the flywheel generator with rectifier, the lead-acid battery bank, and the capacitor bank [11]. A 60 T/100 ms FTMF is achieved based on a 1430 MVA/650 MJ generator with a rectifier at the National High Magnetic Field Laboratory in the USA [12]. The Wuhan National Magnetic Field Center (WHMFC) has achieved a 50 T/100 ms FTMF by 100 MVA/100 MJ generator with a 135MW rectifier [13]. The flywheel generator with rectifier has a favorable ability to control the output voltage by adjusting the trigger angle of the rectifier. However, the flywheel generator is expensive to operate and maintain, and the control method of the rectifier is complicated. Utilizing the battery banks with a bypass circuit of insulated-gate bipolar transistors, a 23.37 T/ 100 ms FTMF is achieved at WHMFC [14]. The battery bank has a stable output voltage, which facilitates the generation of FTMF with high stability. However, the output voltage of the battery bank is relatively

The associate editor coordinating the review of this manuscript and approving it for publication was Zhengqing Yun.

low, which makes it difficult to generate FTMF with high field strength. Additionally, when generating the FTMF with the generator and the battery, the rise time of the current is usually longer than 100 ms, which leads to a considerable temperature rise of the coil before the system reaches the flat-top period. The undesirable temperature rise reduces the pulse width of the FTMF and lengthens the time it takes for the magnet to cool down. A 64 T/10 ms FTMF with 0.3% ripple with coupling capacitors loops is also achieved at WHMFC [15]. A pulsed current with a 26 kA/12 ms flat-top is realized by the capacitor power supply at the Laboratory for Space Environment and Physical Sciences in China [16]. A 60 T/2 ms/82 ppm FTMF is achieved at the Institute for Solid State Physics in Japan. In this system, the main coil is energized by a capacitor bank, and the mini coil is driven by an auxiliary battery to modify the FTMF [17]. In [18], a 44 T/ 1 ms/ <1% FTMF is obtained by capacitors with the scheme of pulse forming network (PFN). The capacitor can output a high discharge current, which is beneficial to generate an FTMF with high field strength. Nevertheless, the coupling capacitors loops and the branch of the mini coil cannot extend the pulse width of the FTMF to tens of milliseconds since the output voltage of the capacitor drops rapidly and uncontrollably. When utilizing PFN to power a magnet, it is necessary to ensure that the parameters of the PFN match the parameters of the load and that the PFN is not flexible for a non-linear variable load like a pulsed magnet. The existing FTMF systems mentioned above are listed in Table 1.

TABLE 1. Main parameters of existing FTMF systems.

Power supply	[Ref.]	Peak (T)	Stability (ppm)	Duration (ms)	Rise Time (ms)
Generator	[12]	60	N/A	100	2000
	[13]	50	5000	100	550
Battery	[14]	23.4	65	100	430
Capacitor	[15]	64	3000	11	13
	[16]	N/A	N/A	12	1
	[17]	60.6	82	2	15
	[18]	44	<10000	1	N/A
Capacitor	This work	50	<7000	70	90

In this paper, an FTMF system powered by a multiple-capacitor power supply (MCPS) which is composed of several paralleled capacitor banks, is proposed. These capacitor banks are charged to the given voltage and discharge successively according to the designed time series to ensure that the output current is stabilized within a certain range during the flat-top period. The MCPS has low maintenance costs, does not need a complicated control method, can output a higher current with a shorter rise time, and can adjust the pulse width of the FTMF effectively by changing the quantity of the capacitor banks. The FTMF generated by the MCPS-powered system has a favorable performance with the magnetic field strength, flat-top pulse width, and stability, which is a meaningful improvement for the field of the FTMF system. The parameters between and within the power supply and the magnet are closely coupled and vary in real-time,

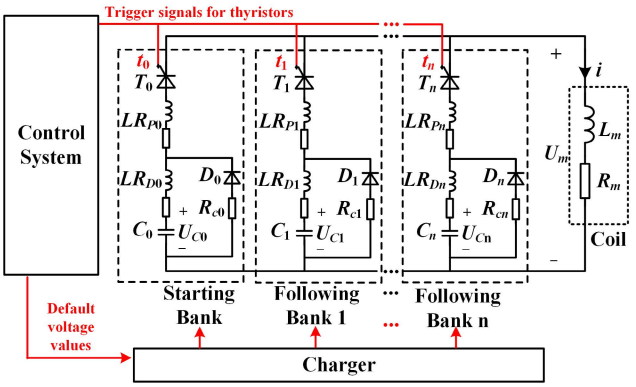

FIGURE 1. Topology of the MCPS.

which poses challenges in the design of the FTMF system. Therefore, a hybrid evolutionary algorithm that combines genetic algorithm (GA) and particle swarm optimization (PSO) is employed to handle the multi-objective optimization problem and calculate the discharge parameters of the MCPS. Based on the optimization results, the FTMF system with optimized parameters are modeled by MATLAB/Simulink and realized by test. The result with the highest field strength is a 50 T/70 ms FTMF with a ripple of less than 0.7 percent, demonstrating the validity of the design.

The rest of this paper is organized as follows. The system configuration is presented in Section II. In Section III, the principle of the FTMF system is analyzed in detail. The optimization process and results are demonstrated in Section IV. Section V presents the test results and discussion. Finally, the conclusion is presented in Section VI.

II. SYSTEM CONFIGURATION OF THE FTMF SYSTEM

A. MULTIPLE-CAPACITOR POWER SUPPLY

Fig. 1 presents the topology of the MCPS. T_0-T_n are the switches. LR_{D0}-LR_{Dn} and LR_{P0}-LR_{Pn} are damping inductors and protect inductors of each capacitor bank. The crowbar circuit of each bank consists of diode D and resistor R_c. L_m and R_m are the inductance and resistance of the magnet, respectively.

The calculated discharge time series t_0-t_n and the initial voltage values of each bank in the MCPS U_{c0}-U_{cn} are saved in the control system. These discharge parameters can be customized according to the parameters of the intended FTMF. Before the discharge process begins, the charger is controlled to charge to the predefined voltage. When the discharge process begins, the control system sends trigger signals to the switches of each bank successively to make them turn on.

According to the opening time-series of the switches, the MCPS is divided into a starting bank and several following banks. The starting bank is the first to discharge, followed by the following banks. The starting bank and following banks are paralleled to form the MCPS. The capacitance of each bank is determined by the capacity of the power supply and the field strength of the intended FTMF.

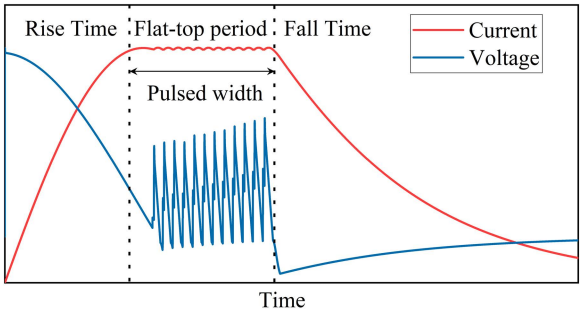

FIGURE 2. Typical output waveform of the FTMF system.

B. PULSED MAGNET

The pulsed magnet is an air-core coil that can be equated to a large inductor and a variable resistance connected in series, and the magnetic field has a linear relationship with the current. The wire composition of the coil can be pure copper or alloys of copper with other metals. The magnet is immersed in liquid nitrogen and pre-cooled to 77 K before discharge. During the discharge process, the resistance of the magnet coil will rise due to the Joule heat, which means the variation of the resistance cannot be overlooked in the analysis of the FTMF system [19]. In addition to Joule heat, the magneto-resistive effect and the skin effect also affect the coil resistance during the pulse generation. Since the discharging period is relatively short, it can be assumed that the current through the magnet is uniformly distributed over the conductor cross-section, the temperature rise is the same in the conductor, and the magnet operates in an ideal adiabatic state to simplify the analysis process [20]. According to the thermal equilibrium, the variation of temperature can be iteratively calculated by

$$\mathrm{d}Q = c(T)m\,\mathrm{d}T = [i(t)]^2 r_m\,\mathrm{d}t = [J(t)]^2\rho(T)V\,\mathrm{d}t \quad (1)$$

where $c(T)$ is the specific heat capacity of the copper, T is the temperature of the magnet, m is the mass of the coil, $i(T)$ is the current of the coil, r_m is the resistance of the coil, $J(T)$ is the current density of the coil, $\rho(T)$ is the resistivity of copper, V is the volume of magnet coil. The specific heat capacity can be obtained by

$$c(T) = 834 - 4007y + 4066y^2 - 1463y^3 + 179.7\,y^4 \quad (2)$$

$$y = \log_{10} T. \quad (3)$$

And the resistivity of copper can be calculated through

$$\rho(T) = -3.14 \times 10^{-9} + 7.2 \times 10^{-11} T. \quad (4)$$

Based on (1)-(4), the variation of magnet resistance in the discharge process can be obtained [21].

III. OPERATING PRINCIPLE OF THE FTFM SYSTEM

Fig. 2 shows the typical output waveform of current and voltage on the coil during the discharge of the FTMF system, and the enlarged image is illustrated in Fig. 3. The entire discharge process consists of three parts: the rise time of the starting bank discharges, the flat-top magnetic field period, and the final fall time.

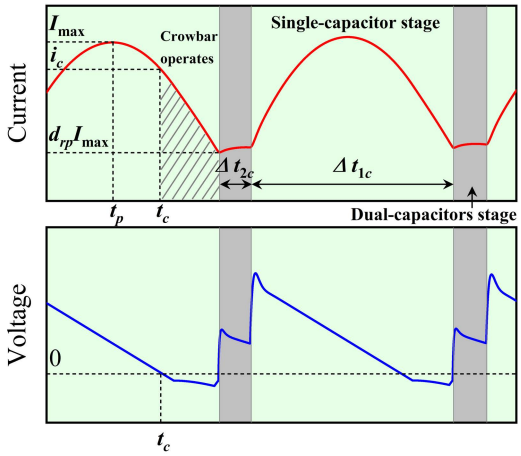

FIGURE 3. Enlarged image of a part of flat-top waveform.

The flat-top period is composed of several pulses. The magnet is powered by a single capacitor bank in a pulse, so these pulses are defined as "single-capacitor stage" (the green section in Fig. 3). The duration of the single-capacitor stage is represented by Δt_{1c}. At t_p, the magnet current reaches peak $I_{\max}$ and then starts to drop. We define d_r as the descent rate of the current drop from peak value in a pulse. When the t_c is reached, the voltage of the magnet drops to zero, and the crowbar circuit begins to operate.

The switch of the subsequent bank is turned on when the magnet current drops to the predefined current $d_{rp}I_{max}$. In this stage, two capacitor banks simultaneously energize the magnet, which is defined as the "dual-capacitors stage" (the gray section in Fig. 3). The duration of the dual-capacitors stage is represented by Δt_{2c}. When the current of the previous bank drops down to zero, the switch of it turns off, and the subsequent bank starts to supply power to the coil alone. The whole system re-enters the single-capacitor stage. As the single-capacitor stage and the dual-capacitors stage appear alternately, an FTMF with desired pulse width is generated.

A. SINGLE-CAPACITOR STAGE

Fig. 4 illustrates the scheme of the circuit in the single-capacitor stage. We assume that the resistance of the magnet is a constant value in the analysis of the circuit to illustrate the physical meaning of each parameter during the discharge process. As shown in Fig. 4(a), the circuit before the crowbar circuit operating is a series RLC circuit. Set $L_1 = L_{d1} + L_{p1} + L_m$ and $R_1 = R_{d1} + R_{p1} + R_m$, the circuit equation is presented as

$$\begin{cases} L_1\dot{i}_1 = -R_1 i_1 + u_1 \\ C_1\dot{u}_1 = -i_1 \end{cases} \quad (5)$$

If this bank is starting bank, the current of coil $i(t)$ can be obtained by

$$\begin{cases} i_{sb}(t) = \dfrac{U_1}{L\omega_{d1}} e^{-\alpha_1 t}\sin(\omega_{d1} t) \\ I_{\max} \approx U_1\sqrt{\dfrac{C_1}{L_1}} \quad (\alpha_1 \ll \omega_1). \end{cases} \quad (6)$$

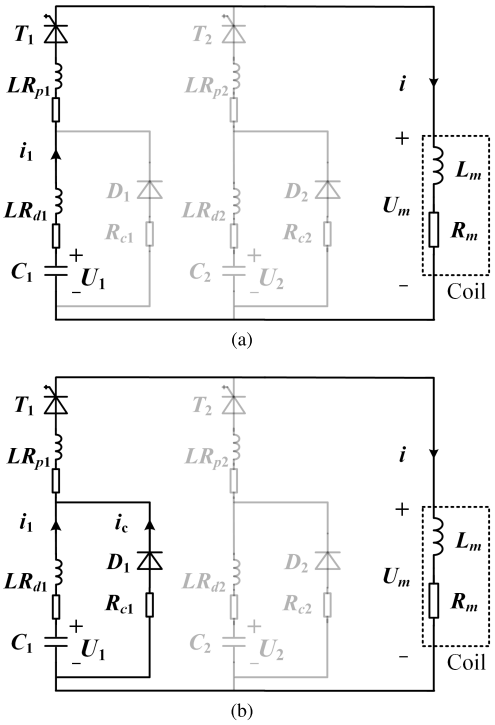

FIGURE 4. Circuit of single-capacitor stage. (a) without crowbar circuit, (b) with crowbar circuit.

where the resonance frequency is $\omega_1 = 1/\sqrt{L_1C_1}$, the damping attenuation is $\alpha_1 = R_1/2L_1$, the frequency $\omega_{d1} = \sqrt{\omega_1^2 - \alpha_1^2}$, and the initial voltage of the capacitor bank is represented by U_1.

The initial state in (5) is not zero for the following banks. Since the duration of the dual-capacitors stage is relatively short, when the variation of current and voltage caused by the previous dual-capacitors stage is overlooked, the initial voltage and initial current in the circuit can be considered as $u_1(0) = U_1$ and $i_1(0) = d_{rp}I_{\max}$. The current of the following bank is presented by solving (5) as

$$i_{fb}(t) = e^{-\alpha_1 t}\frac{\omega_1^2 U_1 C_1 - \alpha_1 d_{rp} I_{\max}}{\omega_{d1}}\sin(\omega_{d1}t) + e^{-\alpha_1 t} d_{rp} I_{\max}\cos(\omega_{d1}t). \quad (7)$$

The output waveforms of the following banks are affected by the capacitance C_1, the initial voltage U_1 and the initial current $d_{rp}I_{\max}$. In the analysis of the relationship between the parameters of the following bank and the waveform of FTMF, we apply two simplifications: setting R_1 in (7) equals zero and ignoring the operating of the crowbar circuit. The equation after simplifying is presented as

$$i_{fb}(t) = U_1\sqrt{\frac{L_1}{C_1}}\sin(\omega_1 t) + d_{rp}I_{\max}\cos(\omega_1 t). \quad (8)$$

The maximum output current of this following bank is

$$I_{fb\max} = \sqrt{\frac{L_1\left(d_{rp}I_{\max}\right)^2 + C_1U_1^2}{L_1}}. \quad (9)$$

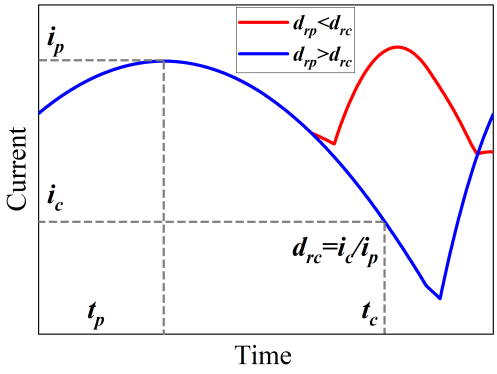

FIGURE 5. Operating conditions of the crowbar.

The duration of its single-capacitor stage Δt_{1c} can be solved by $i_1(0 + \Delta t_{1c}) = d_{rp}I_{\max}$ as

$$\Delta t_{1c} = \sqrt{L_1C_1}\arccos\left[\frac{L_1\left(d_{rp}I_{\max}\right)^2 - C_1U_1^2}{L_1\left(d_{rp}I_{\max}\right)^2 + C_1U_1^2}\right]. \quad (10)$$

According to (9) and (10), some conclusions about the waveform of the following banks can be obtained. Firstly, when $d_{rp}I_{\max}$ is determined, the more stored energy in the following bank leads to a larger $I_{fb\max}$. Secondly, when $I_{\max}$ is determined, the smaller d_{rp} causes a longer Δt_{1c} and larger stored energy. Thirdly, when $d_{rp}I_{\max}$ is determined, the following bank with larger capacitance can extend a longer Δt_{1c}.

When the voltage of the capacitor bank drops to zero at t_c, the crowbar circuit starts to operate. Whether the crowbar circuit operates or not depends on the relationship of magnitude between the descent rate when the crowbar circuit operates d_{rc} and the predefined descent rate d_{rp}. By solving (5), the d_{rc} can be calculated as

$$d_{rc} = \sqrt[\omega_{d1}]{e^{[2\arctan(\omega_{d1}/\alpha_1)-\pi]}}. \quad (11)$$

As demonstrated in Fig. 5, if the predefined descent rate $d_{rp} < d_{rc}$, the system enters the dual-capacitors stage before the crowbar starts to operate. Conversely, the crowbar will operate when $d_{rp} > d_{rc}$. It can be noted that d_{rc} is related to the capacitance, inductance, and resistance in the circuit. Therefore, it is necessary to ascertain whether the crowbar circuit operates at each single-capacitor stage to ensure the accuracy of the calculation.

Since the resistance and inductance of the damping inductor are relatively small, we overlook them to simplify the analysis. The equivalent circuit when the crowbar circuit operates is shown in Fig. 4(b), set $L_2 = L_{p1} + L_m$ and $R_2 = R_{p1} + R_m$ and the circuit equation is presented as

$$\begin{cases} L_2\dot{i} = -R_2 i + u_1 \\ C_1\dot{u}_1 = -i - u_1/R_{c1}. \end{cases} \quad (12)$$

With the initial value $i(0) = I_{L0}$, $u_1(0) = 0$, we can solve (9) to obtain the derivative of magnet current as

$$\dot{i} = \frac{I_{L0}\left(\omega_{d2} - \alpha_2\right)e^{(\omega_{d2}-\alpha_2)(t-t_c)}}{2C_1R_{c1}\omega_{d2}}$$

$$+\frac{I_{L0}\left(\omega_{d2}+\alpha_2\right)e^{-(\omega_{d2}+\alpha_2)(t-t_c)}}{2C_1R_{c1}\omega_{d2}} +\frac{I_{L0}\left(\omega_{d2}-\alpha_2\right)^2e^{(\omega_{d2}-\alpha_2)(t-t_c)}}{2\omega_{d2}} +\frac{I_{L0}\left(\omega_{d2}+\alpha_2\right)^2e^{-(\omega_{d2}+\alpha_2)(t-t_c)}}{2\omega_{d2}}. \tag{13}$$

where the $\omega_2=\sqrt{\left(R_{c1}+R_2\right)/R_{c1}C_1L_2}$, the damping attenuation is $\alpha_2=\left(R_2R_{c1}C_1+L_2\right)/2\,R_{c1}C_1L_2$, the frequency $\omega_{d2}=\sqrt{\omega_2^2-\alpha_2^2}$. According to (13), a larger R_{c1} will make the magnet current drop faster and reach d_{rp} earlier. For increasing the pulse width of the FTMF as long as possible, a smaller R_{c1} is more favorable to be chosen.

B. DUAL-CAPACITORS STAGE

When the switch of the next following bank is turned on, the circuit is illustrated in Fig. 6, and the detailed waveforms of current and voltage is presented in Fig. 7.

If the crowbar circuit of the previous bank is operating at t_{2c1}, the subsequent bank will apply a reverse voltage to the previous bank, causing the crowbar circuit to stop work at t_{2c2}. The circuit between t_{2c1} and t_{2c2} is shown in Fig. 6(a). Set $L_3=L_{p2}+L_{d2}$, $R_3=R_{p2}+R_{d2}$, and overlook the resistance and inductance of the damping inductor, the equation of circuit is presented as

$$\begin{cases} L_{p1}\dot{i}_1=-\left(1/L_{p1}C_1R_{c1}+R_{p1}\right)i_1 \\ +\left(R_3+R_{p1}\right)i_2+R_{p1}i+u_2-u_1 \\ C_1R_{c1}\dot{i}_c=i_1 \\ \left(L_m+L_3\right)\dot{i}_2=\left(L_mR_{p1}/L_{p1}\right)i_1 \\ -\left[L_m\left(R_3+R_{p1}\right)/L_{p1}+R_m+R_3\right]i_2 \\ -\left(L_mR_{p1}/L_{p1}\right)i+\left(L_m/L_{p1}+R_m/R_{c1}\right)u_1 \\ -\left[\left(L_m-L_{p1}\right)/L_{p1}\right]u_2 \\ C_1\dot{u}_1=-i_1 \\ C_2\dot{u}_2=-i_2. \end{cases} \tag{14}$$

Based on (14), the magnet voltage is less than zero in this short period, leading to a higher di_2/dt. Therefore, the voltage on the damping inductor and the protection inductor of the subsequent bank is higher, as shown in Fig. 7.

With the crowbar circuit of previous bank not operating, the circuit is shown in Fig. 6(b). Set $L_4=L_{p1}+L_{d1}$, $R_4=R_{p1}+R_{d1}$, and the circuit equation is presented as

$$\begin{cases} L_x\dot{i}_1=-\left(L_3R_4+L_mR_4+L_3R_m\right)i_1 \\ +\left(L_mR_3-L_3R_m\right)i_2+\left(L_3+L_m\right)u_1-L_mu_2 \\ L_x\dot{i}_2=-\left(L_4R_3+L_mR_3+L_4R_m\right)i_2 \\ +\left(L_mR_4-L_4R_m\right)i_1+\left(L_4+L_m\right)u_2-L_mu_1 \\ C_1\dot{u}_1=-i_1 \\ C_2\dot{u}_2=-i_2 \\ L_x=L_4L_3+L_mL_4+L_mL_3. \end{cases} \tag{15}$$

In the dual-capacitors stage, there is a commutation between the previous bank and the subsequent bank. According to the turn-on and turn-off conditions of the thyristor,

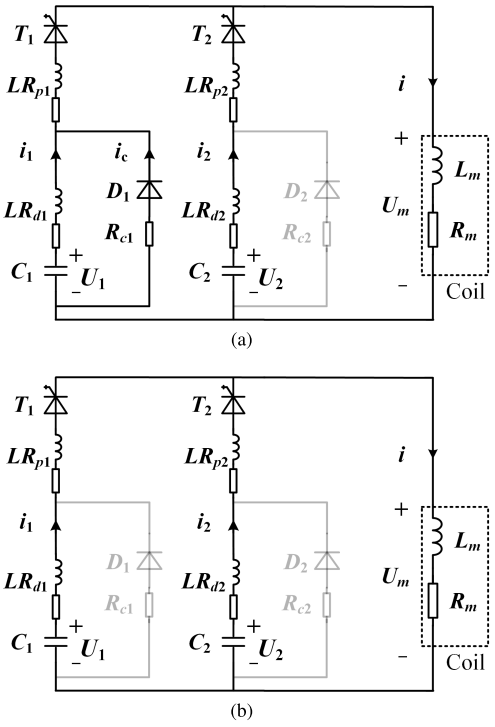

FIGURE 6. Circuit of dual-capacitors stage. (a) with crowbar circuit, (b) without crowbar circuit.

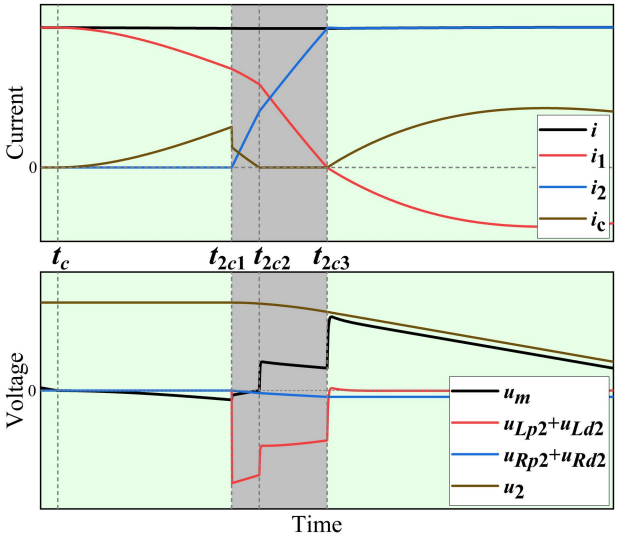

FIGURE 7. Commutation in the dual-capacitors stage. (crowbar of previous bank operates)

the following three conditions need to be satisfied for the following bank to ensure a successful commutation. Firstly, the initial voltage value of the following bank needs to be larger than the current magnet voltage at the beginning of the commutation (i.e. $U_2>u_m(0)$). Secondly, the maximum output current of the following bank needs to be larger than the magnet current during the commutation (i.e. $i_{2\max}>i$). Thirdly, the voltage on the following bank at the end of the commutation needs to be larger than zero during the reverse recovery time of the thyristor of previous bank (i.e. $u_2(t_{2c3}+t_{rr})>0$).

Due to the commutation period being short, we assume the magnet current and the voltage of the previous bank during the commutation is a constant ($d_{rp}I_{max}$ and U_1) for simplifying the analysis. In addition, the operation of crowbar circuit results in a higher average di_2/dt (i.e. higher $i_{2\max}$) during the commutation. Therefore, we assume that the crowbar circuit is not operating when the dual-capacitors stage starts. Based on these assumptions, the equation of commutation is presented as

$$\ddot{u}_2 + \frac{R_4 + R_3}{L_4 + L_3}\dot{u}_2 + \frac{u_2}{C_2\,(L_4 + L_3)} = \frac{U_1 - R_3 d_{rp} I_{\max}}{C_2\,(L_4 + L_3)}. \quad (16)$$

And the conditions for successful commutation can be obtained by solving (16) as

$$\begin{cases} U_2 > u_m(0) \\ U_2 > d_{rp} I_{\max}\sqrt{L_3 + L_4}/\sqrt{C_2} \\ u_2\,(t_{2c3}) \gg 0. \end{cases} \quad (17)$$

where the resonance frequency α_3=$(R_3 + R_4)\,/2\,(L_3 + L_4)$, the damping attenuation ω_3=$1/\sqrt{C_2\,(L_3 + L_4)}$, the frequency ω_{d3}=$\sqrt{\omega_3^2 - \alpha_3^2}$.

The operation of the crowbar circuit of the previous bank causes a larger average di_2/dt during the commutation, Δt_{2c} can be estimated by

$$\Delta t_{2c} \le \frac{1}{\omega_{d3}} \arcsin\left(\frac{d_{rp} I_{\max}}{U_2}\sqrt{\frac{L_3 + L_4}{C_2}}\right) (\alpha_3 \ll \omega_3)\,. \quad (18)$$

The dual-capacitors stage is a transition between two single-capacitor stages, a smaller Δt_{2c} can lead to an increase in the stability of the FTMF if the same I_{max} is ensured at these two single-capacitor stages. According to (9) and (18), a higher initial voltage on the following bank will simultaneously decrease Δt_{2c} and increase the output peak current i_{2max}. Therefore, a reasonable design of parameters for each bank is required in the design of the FTMF system.

When the last dual-capacitors stage is over, the last following bank will energize the magnet alone, and the system will end up discharging in this single-capacitor stage. The entire discharge process of the FTMF system can be calculated by (5), (12), (14), and (15). However, the closed-form solutions of these equations can not be obtained with a variable resistance of magnet based on (1)-(4). In the optimization process, we calculated the parameters of the circuit iteratively with a step size of one microsecond.

IV. OPTIMIZED DESIGNING OF THE FTMF SYSTEM

Based on the analysis in Section III, it is clear that the waveform of FTMF is influenced by the predefined descent rate, the initial voltage on each capacitor bank, the resistance and inductance in the circuit, and the characteristics of the crowbar circuit. There is indeed a strong coupling between and within the variable parameters of the power supply and the magnet during the discharge process. Meanwhile, many constraints need to be considered in the design of the FTMF system. For example, the long pulse and the high field level

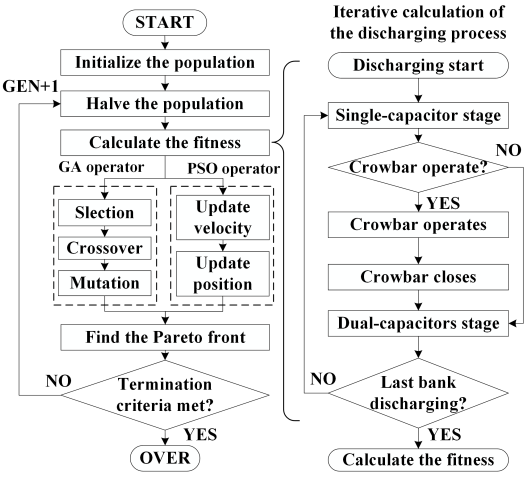

FIGURE 8. Flow chart of GA-PSO hybrid algorithm.

TABLE 2. Parameters of GA-PSO hybrid algorithm.

Quantity	Parameter
Population size	100
Max Generation number	80
Crossover probability P_c	0.85
Mutation probability P_m	0.15
Acceleration constant C_1 and C_2	1.2
Inertia weight w	0.5

will cause the rise of temperature on the magnet. If the temperature exceeds the limits of the materials of the coil, magnet failure will happen [22]. In addition, the capacity and maximum output of the power supply are also part of the constraints. The objectives can also be various such as the field strength, the temperature rise, the stability, and the pulse width of the flat-top. Some of them are conflicting. For example, the setting of d_{rp} causes a trade-off between the pulse width and the stability. Consequently, the simultaneous optimal solution for all objectives does not exist. When designing a specific FTMF system, the requirements of a scientific experiment may make some of the objectives at a specific value or within a certain range. In this case, these constrained parameters are also a part of constraints, and our specific optimization goal is to determine the remaining parameters so that the designed FTMF system not only meets the requirements of scientific experiments but also has better performance on other aspects.

As a result, the designing of the FTMF system with specified objectives under various constraints and initial conditions is indeed a multi-objective optimization problem [23]. An appropriate method for rational design is required.

A. OPTIMIZATION METHOD

The equation of the optimization is described by

$$\vec{y}_i = f\left(\vec{X}_i\right) = \left(-B, -t_{pw}, +e_r, -R_{end}\right) \quad (19)$$

$$\min \vec{Y}_i = \left(\vec{y}_1, \vec{y}_2, \ldots, \vec{y}_n\right) \quad (20)$$

where $\vec{Y}_i$ is the objective vector, B is the magnetic field strength, t_{pw} is the duration time of entire flat-top pulse, e_r is the stability of flat-top field. R_{end} is the resistance of

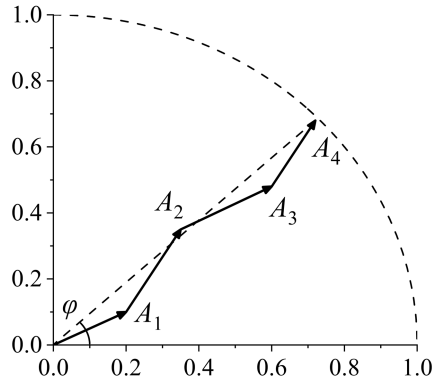

FIGURE 9. Schematic of the basis vector method.

the magnet at the end of discharge, and this value have a positive correlation with the temperature rise of the magnet. The decision vector $\vec{X}_i$ is given by

$$\vec{X}_i = (n, U_{in1}, \ldots, U_{inn}, C_1, \ldots, C_n, t_1, \ldots, t_n, d_{rp}, R_{m0}, L_m, m). \quad (21)$$

where n is the total number of the capacitor banks, U_{in1}-U_{inn} is the initial voltage of each bank, C_1-C_n is the capacitance of each bank, t_1-t_n is the turn-on time of each bank, d_{rp} is the default descent rate of magnet current, R_{m0} is the resistance of the magnet in 77 K environment, L_m is the inductance of the magnet, m is the mass of magnet.

Many algorithms can be employed to solve the multi-objective optimization problem and find the Pareto front [24]. GA has robustness in searching for the global Pareto optimal solution, but its computational speed is slower [25]. PSO converges much sooner than GA due to it does not require operations such as crossover and mutation, but it is easy to fall into local optimum [26]. Considering the running speed and robustness of the algorithm, we finally obtain the Pareto front through the GA-PSO hybrid algorithm. The GA-PSO hybrid algorithm can combine the advantages of both GA and PSO algorithms with retained independence to each other [27], [28]. The flow chart of the GA-PSO hybrid algorithm is shown in Fig. 6. In the hybrid algorithm, we divide the initial population into two parts of equal size and process the separated populations via GA and PSO, and then search the Pareto front between the computed solutions. An iterative calculation in the fitness calculation is used to calculate the entire discharge process based on the analysis mentioned in Section II and Section III. The other parameters of the hybrid algorithm are shown in Table 2.

Each solution in the Pareto front contains information in multiple dimensions. Data visualization is needed in selecting the solution with a relatively optimal performance from the Pareto front [29]. Considering that the data visualization method should be as straightforward as possible, the basis vector method is adopted [30]. The schematic of the basis vector method with four objectives is shown in Fig. 7. After finding the Pareto optimal solution set $\vec{X}$ with r objectives, the basis vector can be obtained by normalizing the fitness on each dimension of the solution. According to the rotation angle $\theta(\vec{X})$, separate basis vectors are rotated and summed and finally mapped to a fold line. In particular, the weighted value $w_k = 1/r$ if the decision-maker has no preferential demand for each objective. The calculation of basis vector is obtained by

$$\theta_i(\vec{X}) = \frac{f_i(\vec{X}) - f_i^{\min}}{f_i^{\max} - f_i^{\min}} \quad (22)$$

$$\vec{A}_r = \left(\sum_{j=1}^{r} w_j \cos\theta_j, \quad \sum_{j=1}^{r} w_j \sin\theta_j \right), \sum_{j=1}^{r} w_j = 1. \quad (23)$$

with larger Euclidean distance $\overline{|OA_r|}$ between the endpoint of the fold line A_r and the O point of the coordinate system, the performance of the solution on each objective is more balanced. And the smaller angle $\angle A_r OX$ between the straight line $\overline{OA_r}$ and the x-axis of the coordinate system, the better the comprehensive performance of the solution. Therefore, we can easily select the best solution from the Pareto front, laying the foundation for the experiment.

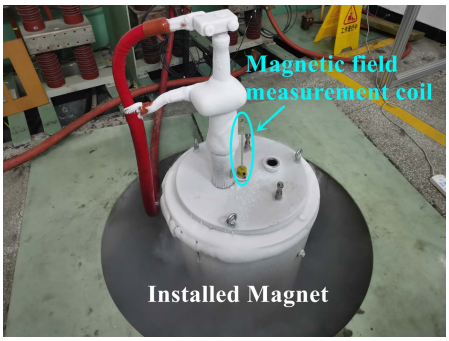

FIGURE 10. Installed 50 T magnet.

TABLE 3. Parameters of pulsed magnet.

Quantity	Parameter
Resistance at 77K, mΩ	168.3
Resistance at 293K, mΩ	1082.5
Inductance, mH	132
Current/Field, A/T	173
Maximum rated current, kA	9.12
Maximum working temperature, K	339
Height, mm	268
Inner radius, mm	19
Outer radius, mm	185.7
Mass of wire, kg	155

B. CONSTRAINTS OF MAGNET AND POWER SUPPLY

Before calculating the optimization, it is essential to clarify the constraints imposed by the actual condition of the magnet and power supply.

To generate the FTMF, WHMFC designs a 50 T pulsed magnet. The wire composition of the magnet is pure copper. The wire size is 3.9 × 5.1 mm; the number of layers is 28; the number of turns in a single layer is 50. Table 3 shows the other parameters of the magnet. The installed magnet with the liquid nitrogen pre-cooling is presented in Fig. 10.

Fig. 11 illustrates the photo and scheme of the capacitor module and the FTMF system composed of capacitor modules. There are sixteen capacitor modules available at

(a)

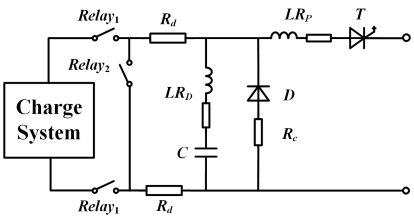

(b)

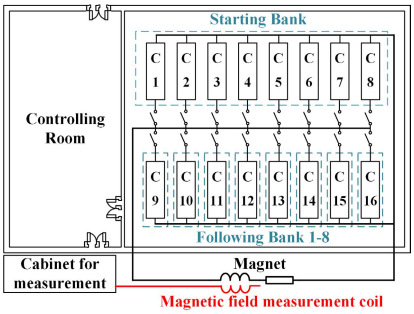

(c)

FIGURE 11. FTMF system composed of capacitor modules (a) photo of single module, (b) scheme of capacitor module, (c) scheme of FTMF system.

TABLE 4. Parameters of capacitor module.

Quantity	Parameter
Capacitance, mF	24×0.16
Nominal voltage, kV	25
Energy density, MJ	1.2
Inductance of LR_D, μH	72/24
Resistance of LR_D, mΩ	112/24
Inductance of LR_p, mH	1
Resistance of LR_p, mΩ	130
Crowbar Resistance, Ω	0.5

WHMFC when building the FTMF system. The capacitor module consists of a charging system, crowbar circuit, twenty-four high-density capacitors, and dumping inductors, thyristors, protect inductors. R_d are resistors that drain energy. The light-triggered thyristors (LTT) with break-over diode function has the advantage of easily isolated triggering by fiber-optic links. Hence, multiple LTTs are connected in series to operate as a switch. The T consists of six series-connected LTTs (T1503N) made by EUPEC Inc. The maximum di/dt, du/dt and i^2t of LTT is 300 A/μs, 2000 V/μs and 15.125 $\times$ 10^6 A^2 s. The crowbar circuit connected in parallel consists of diode D and resistor R_c. The parameters of it are presented in Table 4.

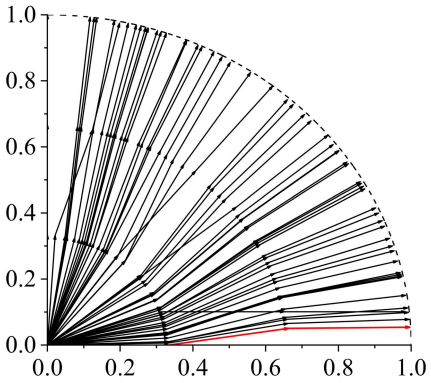

FIGURE 12. Visualized optimization results of 50 T FTMF system.

TABLE 5. Discharge parameters of optimized MCPS in the 50 T FTMF system.

	Initial voltage U_{inn}, (kV)	Discharge time t_n, (ms)
Starting Bank (consists 8 modules)	21.5	0
Following Bank 1-8 (consists 1 modules)	12.48	103
	13.14	110
	13.32	117
	13.12	124
	13.67	131
	13.93	138
	14.25	145
	14.45	152

As indicated in Section II, the capacitance of each capacitor bank (the number of modules in a bank) should be confirmed based on the real capacity of the capacitor power supply. For generating 50 T FTMF, the stored energy of the starting bank needs to be large. If the capacitance of the starting bank is too small, the initial voltage may exceed the maximum rated voltage. Based on (6) and Table 3, the minimum capacitance of starting bank can be calculated as

$$C_{sb} \geq \left(132 \times 10^{-3}\right) \times \frac{50^2 \times 173^2}{25000^2} = 15.8 \text{ mF}. \quad (24)$$

The quantity of modules in starting bank should be at least five. Considering that the initial voltage on the starting bank should not be too high, we determine eight modules connected paralleled are composed of the starting bank.

According to (10), the following bank with larger capacitance can extend the pulse width longer. However, these two parameters do not increase at the same rate. Due to the limited capacity of the capacitors at the WHMFC, each following banks are decided to include only one module.

C. OPTIMIZATION RESULTS

According to the analysis in Section IV-A and IV-B, the multi-objective optimization has three objectives (t_{pw}, e_r and R_{end}). The visualized optimal results of the FTMF system at 50 T level are shown in Fig. 12, and the discharge parameters of the MCPS are shown in Table 5. The selected solution is colored red, which has the relatively largest $\overline{|OA_3|} = 0.998$ and the relatively smallest angle $\angle A_3OX = 3.1°$.

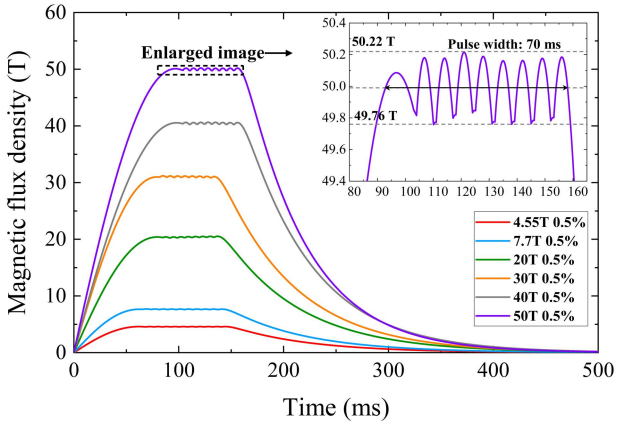

FIGURE 13. Waveforms of simulated FTMF with the stability of 0.5%.

TABLE 6. Parameters of banks in 4.55 T compared experiment.

	Experiment I d_{rp}=0.99		Experiment II d_{rp}=0.98	
	U_{inn} (kV)	t_n (ms)	U_{inn} (kV)	t_n (ms)
Starting Bank (consists 3 modules)	3	0	3	0
Following Bank 1-10 (consists 1 modules)	1.12	68	1.35	70
	1.1	76	1.29	80.2
	1.1	84	1.29	90.4
	1.11	92	1.29	100.6
	1.11	100	1.31	110.8
	1.11	108	1.31	121
	1.11	116	1.31	131.2
	1.11	124	1.31	141.4
	1.11	132	1.31	151.6
	1.11	140	1.31	161.8

In the validation to test the effectiveness of the analysis and the optimization, the other six FTMFs at different magnetic field strength levels driven by MCPS are designed. The optimal solutions are obtained by the GA-PSO hybrid algorithm. The parameters of the magnet are illustrated in Table 3. In the case of starting bank with initial output of 3 kV and 5 kV, starting bank contains three modules, and there are ten following banks; in the case of the target field strength of 20 T and 30 T, the starting bank contains five modules and there are eight following banks; in the case of the target field strength of 40 T, the starting bank contains eight modules and there are eight following banks.

The designed FTMF systems are modeled in MATLAB/Simulink. As presented in Fig.13, the 50 T FTMF has maximum and minimum values during the flat-top pulse period in the simulation are 50.3 T and 49.8 T. The stability of the magnetic field is less than 0.5%. The resistance of the coil after the discharge process in the simulation changes from 168 mΩ to 722 mΩ.

V. EXPERIMENT AND DISCUSSION

In order to verify our analysis of the MCPS circuit in Section III, We conduct two experiments with the same initial voltage U_{in1}=3 kV of starting bank but different d_{rp}. The discharge parameters of the two experiments are presented in Table 6, and a comparison of the waveforms is shown in Fig. 14. Experiment I generated a 4.55 T FTMF with a

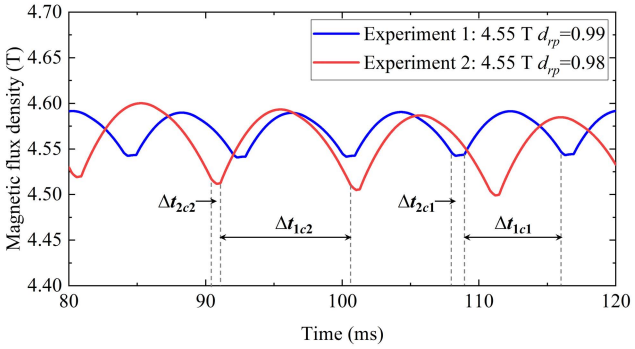

FIGURE 14. Comparison of two experimental waveforms with 4.55 T in the flat-top period.

TABLE 7. Experimental results of generated FTMFs.

U_0 (kV)	Banks	Rise time (ms)	Field strenth (T)	Pulse width (ms)	Stability
3	3+10*1	58	4.55	90	0.50%
3	3+10*1	58	4.55	114	1.05%
5	3+10*1	58	7.6	93	0.50%
10.1	5+8*1	75	20.1	63	0.50%
15.9	5+8*1	75	30.5	67	0.50%
17	8+8*1	92	40.3	68	0.60%
21.5	8+8*1	92	50	70	0.70%

stability of 0.5% and a pulse width of 90 ms, Δt_{1c1}=7.1 ms and Δt_{2c1}=0.95 ms. Experiment II generated a 4.55 T FTMF with the stability of 1.05% and a pulse width of 114 ms, Δt_{1c2}=9.5 ms and Δt_{2c2}=0.7 ms. We can conclude that smaller d_{rp} does cause the pulse width of the FTMF longer and the pre-stored energy of each following bank larger; the larger initial voltage of the following bank does cause a shorter Δt_{2c}. The analysis based on (9), (10), and (18) is valid.

Next, the 7.7 T, 20 T, 30 T, and 40 T FTMF experiments with designed stability 0.5% are conducted. For the experiment of generated FTMF with 50 T, we firstly performed a 50 T single pulse experiment to improve the accuracy of the experimental results. This experiment is used to calibrate the current-to-field ratio of the magnet and the stray inductance and resistance presented in the experimental environment. The parameters of the discharge calculation process are revised in the algorithm based on the results of the single pulse experiment. After the single pulse experiment, the test of the FTMF system is achieved, and a 50 T/70 ms FTMF is obtained. During the flat-top pulse period, the maximum and minimum values are 50.15 T and 49.75 T. The stability of the magnetic field is 0.7 %. The resistance of the coil after the discharge process changes from 168 mΩ to 772 mΩ. The main parameters of the above experiments are shown in Table 7, and the waveforms of the generated FTMF are shown in Fig. 15(a).

It is noted that the stability of the experimental FTMF for 40T and 50T is different from the simulation results, and the reasons for this situation need to be analyzed. The comparison of the experimental and the simulated waveform in the flat-top period with the enlarged image is presented in Fig.15(b). The experimental waveform decreases faster than the simulated waveform in the second half, resulting in poor

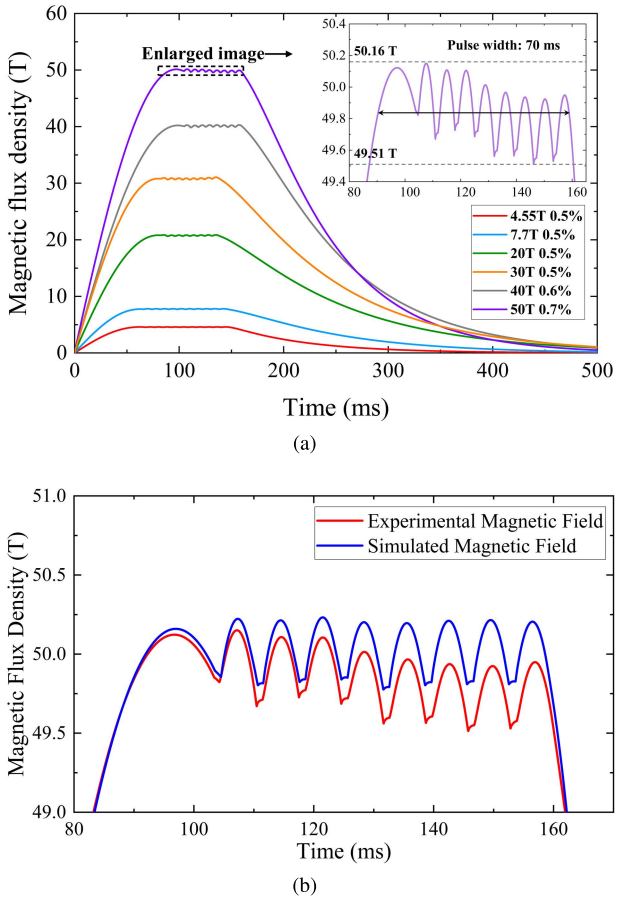

FIGURE 15. **Waveforms of experimental FTMFs. (a) figure of waveforms, (b) comparison of 50 T FTMF between the simulation and the experiment.**

stability. The FTMF system we designed is an open-loop system, and small changes in the power supply and magnet parameters can result in a large variety of outcomes. Therefore, there are inconsistencies between the system parameters in the simulation model and the experiment. We examine various aspects of the operation of the system and came up with the two main reasons for this inconsistency described below.

Firstly, the resistance of the magnet has inconsistency between the simulation and experiment. The magneto-resistive effect and the skinning effect are not considered for simplification in Section II. However, with high magnetic field strength and longer pulse width, the magnitude of this effect also increases [21]. Therefore, the stability of the FTMF generated by the 40 T and 50 T experiments do not meet the expectation. As mentioned above, the resistance of the magnet after discharging is 722 mΩ in simulation and 772 mΩ in the experiment. The resistance increased in the experiment is larger than that calculated by the thermal model in Section II.

Secondly, the initial voltage of the following banks has inconsistency between the simulation and experiment. The charging system for all capacitor modules at WHMFC can only be activated simultaneously and operates with the constant current mode. It means that capacitor banks with different default initial voltages take different amounts of time to complete charging. While waiting for the other capacitor modules to be discharged, the voltage on the charged capacitor module decreases progressively. Due to the initial voltage of starting bank being substantially higher than that of the following banks, the voltage on the following banks is lower than the default value when the discharge process begins.

Based on the above analysis, the stability of the FTMF can be improved in the following three ways. Firstly, incorporating the additional resistance growth caused by the magneto-resistive effect and the skinning effect into the algorithm. Secondly, modifying the charging program in the control system to ensure that each capacitor bank completes charging simultaneously. Thirdly, adding an auxiliary power supply paralleled with MCPS which can be current-controlled to compensate the magnetic field.

VI. CONCLUSION

The FTMF system powered by MCPS can generated FTMF with short rise time, high field strength, long pulse width, certain stability and low cost. Appling the multi-objective optimized model and the GA-PSO hybrid algorithm, the scheme of FTMF system based on the existing capacitor power supply at WHMFC is obtained. A series of FTMFs at different magnetic strength level are modelled in simulation and realized in experiment, the result with highest field strength is a 50 T/70 ms FTMF with a ripple of less than 0.7 percent. The simulated and experimental results validates the availability of the scheme and lay a foundation to future research of the FTMF.

REFERENCES

[1] S. Ogawa, T.-M. Lee, A. S. Nayak, and P. Glynn, "Oxygenation-sensitive contrast in magnetic resonance image of rodent brain at high magnetic fields," *Magn. Reson. Med.*, vol. 14, no. 1, pp. 68–78, 1990.

[2] J. Haase, M. Kozlov, K.-H. Müller, H. Siegel, B. Büchner, H. Eschrig, and A. Webb, "NMR in pulsed high magnetic fields at 1.3 GHz," *J. Magn. Magn. Mater.*, vol. 290, pp. 438–441, Apr. 2005.

[3] T. Maly, G. T. Debelouchina, V. S. Bajaj, K.-N. Hu, C.-G. Joo, M. L. Mak-Jurkauskas, J. R. Sirigir, P. C. A. van der Wel, J. Herzfeld, R. J. Temkin, and R. G. Griffin, "Dynamic nuclear polarization at high magnetic fields," *J. Chem. Phys.*, vol. 128, no. 5, 2008, Art. no. 02B611.

[4] F. Weickert, B. Meier, S. Zherlitsyn, T. Herrmannsdörfer, R. Daou, M. Nicklas, J. Haase, F. Steglich, and J. Wosnitza, "Implementation of specific-heat and NMR experiments in the 1500 ms long-pulse magnet at the Hochfeld–Magnetlabor Dresden," *Meas. Sci. Technol.*, vol. 23, no. 10, 2012, Art. no. 105001.

[5] L. J. Campbell, H. J. Boenig, D. G. Rickel, J. D. Rogers, J. B. Schillig, J. R. Sims, P. Pernambuco-Wise, H. J. Schneider-Muntau, and L. Van Bockstal, "Design and analysis of high-field quasi-continuous magnets," *IEEE Trans. Magn.*, vol. 30, no. 4, pp. 2222–2225, Jul. 1994.

[6] H. Xiao, Y. Ma, Y. Lv, T. Ding, S. Zhang, F. Hu, L. Li, and Y. Pan, "Development of a high-stability flat-top pulsed magnetic field facility," *IEEE Trans. Power Electron.*, vol. 29, no. 9, pp. 4532–4537, Sep. 2014.

[7] H. F. Ding, C. X. Jiang, T. H. Ding, Y. Xu, L. Li, X. Z. Duan, Y. Pan, and F. Herlach, "Prototype test and manufacture of a modular 12.5 MJ capacitive pulsed power supply," *IEEE Trans. Appl. Supercond.*, vol. 20, no. 3, pp. 1676–1680, Jun. 2010.

[8] H. Ding, W. Liu, X. Duan, L. Li, and F. Herlach, "Design and analysis of a combined power supply for high-field quasi-continuous magnets," *IEEE Trans. Appl. Supercond.*, vol. 22, no. 3, Jun. 2012, Art. no. 5400904.

[9] H. Ding, Y. Huang, J. Zhou, Y. Lv, X. Fang, Z. Zhao, T. Ren, H. Li, and X. Xie, "Design of a hybrid power supply for a 65 T quasi-continuous high magnetic field with a dual-coil magnet," *IEEE Trans. Appl. Supercond.*, vol. 28, no. 3, pp. 1–5, Apr. 2018.
[10] D. N. Nguyen, J. Michel, and C. H. Mielke, "Status and development of pulsed magnets at the NHMFL pulsed field facility," *IEEE Trans. Appl. Supercond.*, vol. 26, no. 4, pp. 1–5, Jun. 2016.
[11] L. Li, Y. L. Lv, H. F. Ding, T. H. Ding, X. T. Han, H. X. Xiao, Y. Xu, G. B. Wang, Y. Yuan, F. Jiang, Q. Q. Sun, X. Z. Duan, Y. Pan, and T. Peng, "Short and long pulse high magnetic field facility at the Wuhan national high magnetic field center," *IEEE Trans. Appl. Supercond.*, vol. 24, no. 3, pp. 1–4, Jun. 2014.
[12] J. Schillig, H. Boenig, M. Gordon, C. Mielke, D. Rickel, J. Sims, J. Martin, and R. Williams, "Operating experience of the United States National High Magnetic Field Laboratory 60 T long pulse magnet," *IEEE Trans. Appl. Supercond.*, vol. 10, no. 1, pp. 526–529, Mar. 2000.
[13] H. Ding, Y. Yuan, Y. Xu, C. Jiang, L. Li, X. Duan, Y. Pan, and J. Hu, "Testing and commissioning of a 135 MW pulsed power supply at the Wuhan national high magnetic field center," *IEEE Trans. Appl. Supercond.*, vol. 24, no. 3, pp. 1–5, Jun. 2013.
[14] S. Zhang, Z. Wang, T. Ding, H. Xiao, J. Xie, and X. Han, "Realization of high-stability flat-top pulsed magnetic fields by a bypass circuit of IGBTs in the active region," *IEEE Trans. Power Electron.*, vol. 35, no. 3, pp. 2436–2444, Mar. 2020.
[15] S. Wang, T. Peng, F. Jiang, S. Jiang, S. Chen, L. Deng, R. Huang, and L. Li, "Upgrade of the pulsed magnetic field system with flat-top at the WHMFC," *IEEE Trans. Appl. Supercond.*, vol. 30, no. 4, pp. 1–4, Jun. 2020.
[16] E. Peng, W. Ling, A. Mao, J. Guan, X. Ma, H. Li, Z. Yu, and M. Ding, "A pulsed power supply based on an optimized SFPFN scheme producing large currents with a flat top on a heavily inductive load," *IEEE Trans. Power Electron.*, vol. 36, no. 10, pp. 11221–11233, Oct. 2021.
[17] Y. Kohama and K. Kindo, "Generation of flat-top pulsed magnetic fields with feedback control approach," *Rev. Sci. Instrum.*, vol. 86, no. 10, 2015, Art. no. 104701.
[18] G. Dworschak, F. Haberey, P. Hildebrand, E. Kneller, and D. Schreiber, "Production of pulsed magnetic fields with a flat pulse top of 440 k0e and 1 msec duration," *Rev. Sci. Instrum.*, vol. 45, no. 2, pp. 243–249, 1974.
[19] T. Peng, L. Li, and F. Herlach, "Development of pulsed magnets at WHMFC," *IEEE Trans. Appl. Supercond.*, vol. 20, no. 3, pp. 652–655, Jun. 2010.
[20] Y. Song, T. Peng, L. Li, Y. Lv, and L. Qiu, "Electrical and thermal modeling of pulsed magnets using finite element analysis," *IEEE Trans. Appl. Supercond.*, vol. 20, no. 3, pp. 1785–1789, Jun. 2010.
[21] F. Herlach, "Pulsed magnets," *Rep. Prog. Phys.*, vol. 62, no. 6, p. 859, 1999.
[22] H. Li and H. Ding, "Modeling and multi-objective design optimization of quasi-continuous high magnetic field systems," *Prog. Electromagn. Res.*, vol. 139, pp. 353–372, 2013.
[23] K. Deb, "Multi-objective optimization," in *Search Methodologies*. Boston, MA, USA: Springer, 2014, pp. 403–449.
[24] C. A. C. Coello, G. B. Lamont, and D. A. V. Veldhuizen, "Mop evolutionary algorithm approaches," in *Evolutionary Algorithms for Solving Multi-Objective Problems*, 2nd ed. Boston, MA, USA: Springer, 2007, pp. 61–130.
[25] G. D. Edward, *Genetic Algorithms in Search, Optimization, and Machine Learning*. Reading, MA, USA: Addison-Wesley, 2002.
[26] S. J. Habib and B. S. Al-Kazemi, "Comparative study between the internal behavior of GA and PSO through problem-specific distance functions," in *Proc. IEEE Congr. Evol. Comput.*, vol. 3, Sep. 2005, pp. 2190–2195.
[27] X. H. Shi, Y. C. Liang, H. P. Lee, C. Lu, and L. M. Wang, "An improved GA and a novel PSO-GA-based hybrid algorithm," *Inf. Process. Lett.*, vol. 93, no. 5, pp. 255–261, 2005.
[28] S. Jeong, S. Hasegawa, K. Shimoyama, and S. Obayashi, "Development and investigation of efficient GA/PSO-HYBRID algorithm applicable to real-world design optimization," *IEEE Comput. Intell. Mag.*, vol. 4, no. 3, pp. 36–44, Aug. 2009.
[29] I. Kalamaras, A. Drosou, and D. Tzovaras, "Multi-objective optimization for multimodal visualization," *IEEE Trans. Multimedia*, vol. 16, no. 5, pp. 1460–1472, Aug. 2014.
[30] B. Xiaojun, L. Bo, and C. Yan, "Visualization of high dimension multi-objective of rotation basis based on interactive decision making," *J. Comput.-Aided Des. Comput. Graph.*, vol. 26, no. 5, pp. 739–746, 2014.

DAKE LI received the B.S. degree in electrical engineering from Southeast University, Nanjing, China, in 2014. He is currently pursuing the Ph.D. degree in electrical engineering with the Huazhong University of Science and Technology, Wuhan, China.

His research interests include high-parameter pulsed magnetic fields and application of pulsed power supply.

HONGFA DING received the B.S. degree in electrical engineering and the Ph.D. degree from the Huazhong University of Science and Technology, Wuhan, China, in 1995 and 2002, respectively.

From 2001 to 2002, he was a Visiting Scholar with Liverpool University. Since 2007, he has been a Professor with the School of Electrical and Electronic Engineering and the Wuhan National High Magnetic Field Center, Huazhong University of Science and Technology. His research interests include the application of power electronics in power systems, pulsed power technology, and pulsed strong magnetic field technology applications.

YUCHAO FANG received the B.S. degree in electrical engineering from Tianjin University, Tianjin, China, in 2017, and the M.S. degree in electrical engineering from the Huazhong University of Science and Technology, Wuhan, China, in 2020. He is currently pursuing the Ph.D. degree in electrical engineering with Zhejiang University, Hangzhou, China.

His research interests include high-parameter pulsed magnetic fields and the control of electric motor.

SONG ZHANG received the B.S. degree in electrical engineering from Wuhan University, Wuhan, China, in 2017.

He is currently an Experimenter with the Wuhan National High Magnetic Field Center.

DAIYUAN PAN received the B.S. degree in electrical engineering from the Huazhong University of Science and Technology, Wuhan, China, in 2019, where he is currently pursuing the M.S. degree in electrical engineering.

His research interests include high-parameter pulsed magnetic fields and application of pulsed power supply.